ICAS 2020 SHANGHAI
International Council of the Aeronautical Sciences
32nd Congress of the International Council of the Aeronautical Sciences
September 6-10, 2021
Pudong Shangri-La, Shanghai, China

NUMERICAL SIMULATION STUDY ON BOUNDARY LAYER FLOW AND DRAG REDUCTION CHARACTERISTICS OF RIBLETS

Shuya Du[1], Run Pang[2], Weimin Sang[1] & Guangjun Yang[1]

[1] School of Aeronautics, Northwestern Polytechnical University, Xi'an 710072, China
[2]AVIC Xi'an Flight Automatic Control Research Institute, Xi'an Shannxi 710065, China

Abstract

Turbulent drag reduction is a hot issue in the research of fluid mechanics. Among various turbulent drag reduction methods, riblet is widely concerned due to its simple structure and convenient use. Although the drag reduction effect of riblet has been confirmed by a lot of experiments, there is no unified theory of the drag reduction mechanism of riblets due to limitations of experiment measurement methods. In this paper, large eddy simulation (LES) method is adopted to numerically study the effect of riblets on the turbulent boundary layer. The accuracy of the numerical result is verified by comparing it to the results of direct numerical simulation (DNS). Based on experiment results, flow field parameters of the turbulent boundary layer over riblets are analyzed, such as integral statistics, first-order statistics, and second-order statistics.

Keywords: Turbulent drag reduction; Large eddy simulation; Turbulent boundary layer; Turbulent channel flow; Riblets

1. Introduction

In recent years, commercial aviation has developed vigorously. For aircraft oriented to commercial applications, it is critical to reducing operating costs. Generally, fuel costs account for 30% to 50% of flight operating costs. Aircraft fuel consumption is mainly devoted to overcoming drag generated during the cruise. Take Boeing 737 as an example, 1% drag of each aircraft is equivalent to additional 15000 gallons of aviation fuel per year[1]. In subsonic cruise, friction drag usually accounts for 50% of total drag. Therefore, the reduction of friction drag could generate substantial commercial benefits.

Drag reduction methods in fluid mechanics can be divided into two categories: active drag reduction and passive drag reduction. Compared with active drag reduction, the passive drag reduction method is more convenient to implement. Initially, it was found that animals' skin has many microstructures. There are many streamwise riblets on sharks' skin, which can reduce friction drag[2]. Not only sharks, but birds have also developed surface structures with drag-reducing properties[3].

As early as the 1970s, researchers began to study riblets. In NASA Langley Research Center, Walsh[4][5][6][7] conducted a lot of experiments. Walsh found that V-shaped riblets have the best drag reduction effect, and could achieve around a 6% drag reduction rate under transonic conditions. After that, Bechert[8], Bacher[9] and Choi[10] conducted similar experiments and proposed different theories about the drag reduction mechanism of riblets.

Because riblets mainly affect the flow field in the near wall region of the turbulent boundary layer, flow field parameters in this area are difficult to be obtained in the experiment. Therefore, researchers try to use numerical simulation methods to investigate the drag reduction mechanism of riblets. As early as 1991, Chu[11] used the spectrum method to study the drag reduction effect of riblets on laminar, transition and turbulent flow. Numerical results show that riblets have a drag reduction effect only under transition and turbulent conditions, and riblets could suppress turbulence intensity and

Reynolds stress. After that, Choi[12] used direct numerical simulation (DNS) method to simulate the drag reduction effect of V-shaped riblets. It was found that drag-reducing riblets restrict the location of streamwise vortices so that only the tip of riblets is exposed to high-speed fluid. If riblets' spacing is too large, streamwise vortices could move inside riblet valleys, so that most area of riblets is exposed to high-speed fluid.

Martin[13] used large eddy simulation (LES) method to simulate boundary layer flow over knife-shaped riblets. It was found that when the average diameter of streamwise vortices is 1.5 times larger than riblets' spacing, surface friction drag is decreased. This result supports Choi's explanation of the drag reduction mechanism of riblets. Ng[14] used DNS method to study flow characteristics of drag-increasing and drag-decreasing riblets. Ng found that both types of riblets can effectively suppress streamwise velocity fluctuation, but drag-reducing riblets also suppress normal and spanwise velocity fluctuation, while drag-increasing riblets amplify above two types of velocity fluctuation.

Since riblets' size and aircraft's size often differ by several orders of magnitude, it is difficult to directly arrange riblets on aircraft to numerically study their drag reduction effect. In this regard, Mele[15] proposed using Wilcox rough wall model to model the effect of riblets on the flow field. In recent years, riblet drag reduction technology began to be applied in engineering practice. In 1989, researchers covered 70% of Airbus A320 fuselage with riblet films, and finally achieved a drag reduction rate of 2%. Later, people arranged triangular riblets on the surface of a submarine, and finally got a net drag reduction of 1.2%[16]. Literature[17] made a review about riblets drag reduction technology.

This paper adopts large eddy simulation method to study turbulent boundary layer flow over triangular riblets and analyzes flow field parameters such as integral statistics, first-order statistics and second-order statistics of numerical results to investigate the drag reduction mechanism of riblets and summarize the drag reduction laws.

2. Verification of numerical methods

2.1 Computational domains

According to previous numerical simulation[12] and experiment[8] results, the computational domain in this paper is set into channel flow as shown in Figure 1, with dimensions $L_x \times L_y \times L_z$. The periodic boundary condition is adopted in streamwise (X) and spanwise (Z) directions. The upper surface AEGC and lower surface BFHD adopt no-slip wall boundary conditions. In the validation example, the upper and lower walls are both smooth flat plates. When simulating the flow field over riblets, riblets are arranged on the lower wall, and the flow field parameters of upper and lower walls are compared to investigate the effect of riblets on the flow field.

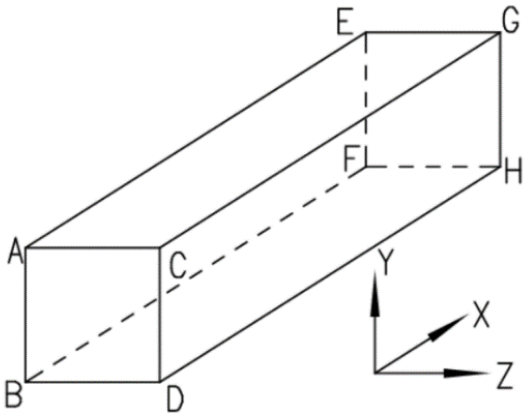

Figure 1 – Computational domain.

In addition to boundary conditions, the adequate computational domain size is also critical. Whether computational domain size is appropriate or not, researchers have developed different test methods and empirical theories. For example, Kim[18] pointed out that for periodic flow fields, the method of

detecting correlation between two points can be used to verify whether computational domain size is appropriate. Jimenez pointed out[13] that for the computational domain shown in Figure 1, the non-dimensional size in spanwise direction should be larger than 100, and in streamwise direction should be larger than 300. Zhang[19] studied the influence of computational domain size on numerical results and pointed out that the computational domain with dimensions of $2\pi\delta\times2\delta\times2\delta$ in X, Y, and the Z direction is appropriate, which δ refers to half of the channel height.

Taking channel height as reference length and bulk velocity as reference velocity, the Reynolds number is 5600 which is the same as Kim[18]. The computational domain in this paper has a non-dimensional length of 1800 in the X direction, and a non-dimensional length of 360 in Y and Z directions, both of which meet the requirements of Jimenez and Zhang.

It is generally believed that in large eddy simulation, the grid resolution must meet $\Delta x^+ < 40$, $\Delta y^+_{min} < 1$ and $\Delta y^+_{max} < 20$, $\Delta z^+ < 20$ [19]. In the validation example, uniform grids are adopted in streamwise and spanwise directions, and grids in normal direction are stretched towards the wall. The number of grids in X, Y and Z directions are 150, 80, 80 respectively. The non-dimensional normal spacing of the first grids near the wall is 0.18, and the maximum spacing is 13. The non-dimensional streamwise and spanwise spacing of grids are 12 and 4.6. In LES method, the dynamic Smagorinsky-Lilly model is used and pressure gradient in the X direction is specified. The non-dimensional time step is taken as 0.001, and the total integration time is taken as 100.

2.2 Numerical Result

Table 1 shows the comparison between the drag coefficient obtained by LES method and DNS result. It can be seen that LES method could predict the drag of smooth plate accurately. Figure 2 shows the comparison between velocity profiles obtained by different numerical methods. Both of them are in good agreement.

Table 1 Comparison of the drag coefficient.

Numerical Method	Drag Coefficient（$\times10^{-3}$）	Relative Error
DNS	8.18	
LES	8.01	2.08%

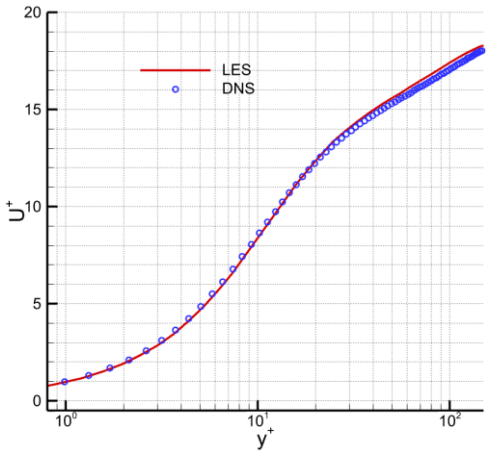

Figure 2 – Time-averaged velocity profile in the turbulent boundary layer.

Figure 3(a) shows the distribution of root-mean-square velocity fluctuation in X, Y, and Z directions. It can be seen that velocity fluctuation distribution is in good agreement with DNS result. Figure 3(b) shows the distribution of Reynolds shear stress, and the LES results are in good agreement with DNS results.

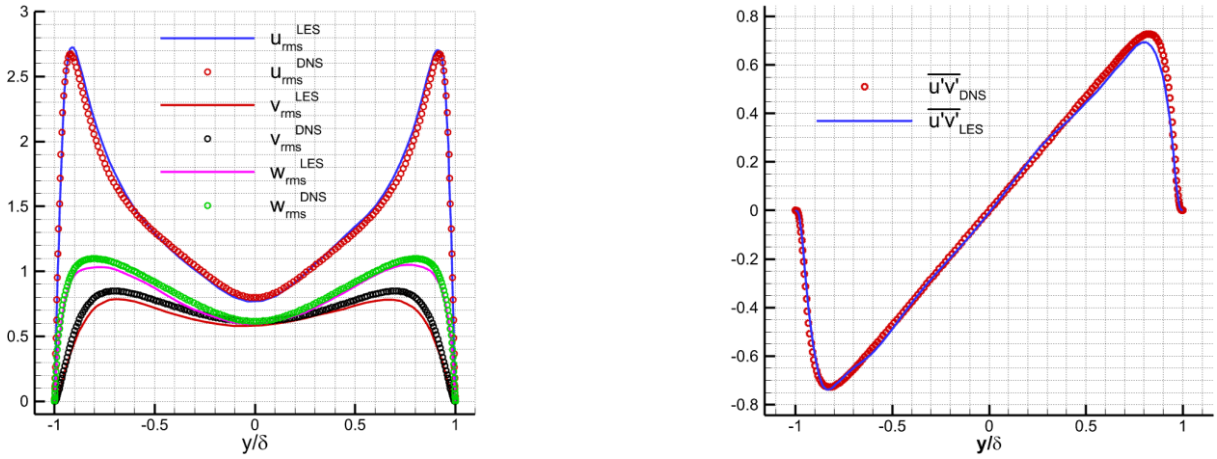

(a) Root mean square velocity fluctuations (b) Reynolds stress

Figure 3 – Distribution of second-order statistics in the turbulent boundary layer.

In the analysis of turbulent flow, quadrant analysis is a very useful method. The quadrant analysis method divides the Reynolds stress into four quadrants according to signs of velocity fluctuation in the X and Y direction. Figure 4 shows the distribution of Reynolds stress in different quadrants and compares it with the DNS results. It can be seen that Q2 and Q4 events dominate the generation of Reynolds stress, and Q4 event dominates in the near-wall region.

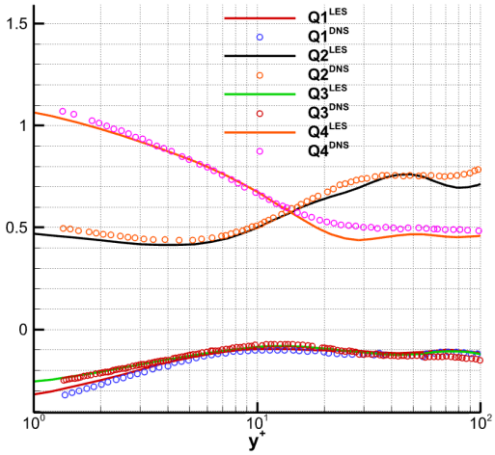

Figure 4 – Distribution of Reynolds stress in different quadrants.

3. Numerical simulation of turbulent boundary layer flow over triangular riblets

3.1 The geometry of triangular riblets

For triangular riblets, there are abundant experiment data. The drag reduction characteristic of triangular riblets is shown in Figure 5[8]. The abscissa s^+ is the non-dimensional spacing of riblets, which is defined as:

$$s^+ = \frac{\rho u_\tau s}{\mu} \tag{1}$$

In equation (1), u_τ is defined as the shear velocity of the smooth flat plate under the same flow condition. When $s^+ < 18$ the drag reduction effect of riblets increases with the increase of s^+. When $s^+ > 18$ the drag reduction effect of riblets decreases with the increase of s^+. In this paper, three kinds of riblets with typical flow characteristics were selected: $s^+ = 9, s^+ = 18, s^+ = 36$. Among them, $s^+ = 18$ have the best drag reduction effect. The drag reduction effect of $s^+ = 9$ riblets is reduced, and $s^+ = 36$ riblets have the drag increasing effect. The geometry of triangular riblets is shown in

Figure 5. The distribution of computational grids over the riblet surface is shown in Figure 6.

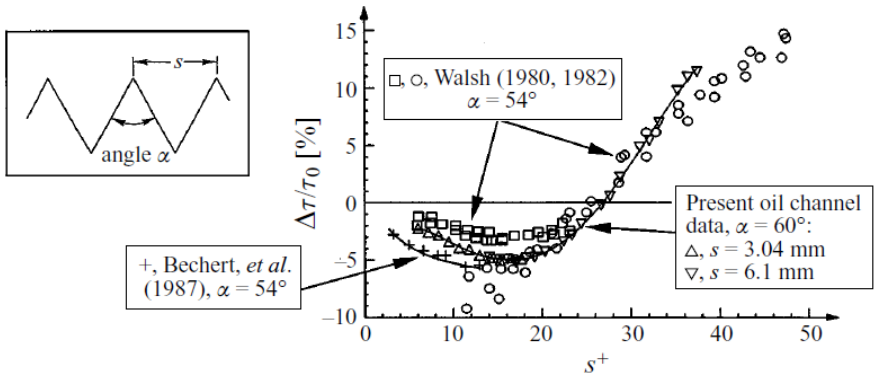

Figure 5 – Drag reduction characteristics of triangular riblets.

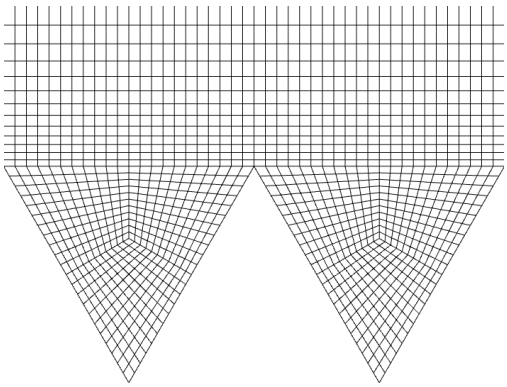

Figure 6 – Distribution of computational grids over riblet surface.

3.2 Integral statistics and first-order statistics

Table 2 shows the numerical results of the drag reduction rate of three kinds of riblets and compares them with the experiment data[8]. Table 3 shows the direct numerical simulation results of Choi et al.[12] and Li et al.[22] on similar-sized triangular riblets. It can be seen that although there is a discrepancy between numerical results and experimental data, the overall trend is in good agreement. By comparing with DNS results, it can be seen that the LES results in this paper are in good agreement with DNS results. In the column of drag reduction rate, the negative value represents drag decrease, and the positive value represents drag increase. The drag reduction rate (DR) is defined as:

$$DR = \frac{F_{riblets} - F_{smooth}}{F_{smooth}} \times 100\% \tag{2}$$

In equation (3-2), $F_{riblets}$ represents the drag of the riblet surface, and F_{smooth} represents the drag of the smooth surface.

Table 2 Drag reduction rate of triangular riblets.

s^+	Drag Reduction Rate	
	Numerical results	Experiment results
9	-3.1%	-3.4%
18	-5.9%	-4.9%
36	+9.5%	+10.3%

Table 3 Comparison of numerical results.

s^+	Drag Reduction Rate		
	Numerical results (LES)	Choi (DNS)	Li (DNS)
18	-5.9%	-6%	-9%
36	+9.5%	+12%	+6.5%

Figure 7 shows the time-averaged velocity profile at the valley and tip of three kinds of triangular riblets and compares them with the velocity profile of the smooth surface. It can be seen that the velocity profile of drag-increasing riblets is significantly lower than that of smooth surface in logarithmic region, while the velocity profile of drag-decreasing riblets is significantly higher than that of drag-increasing riblet.

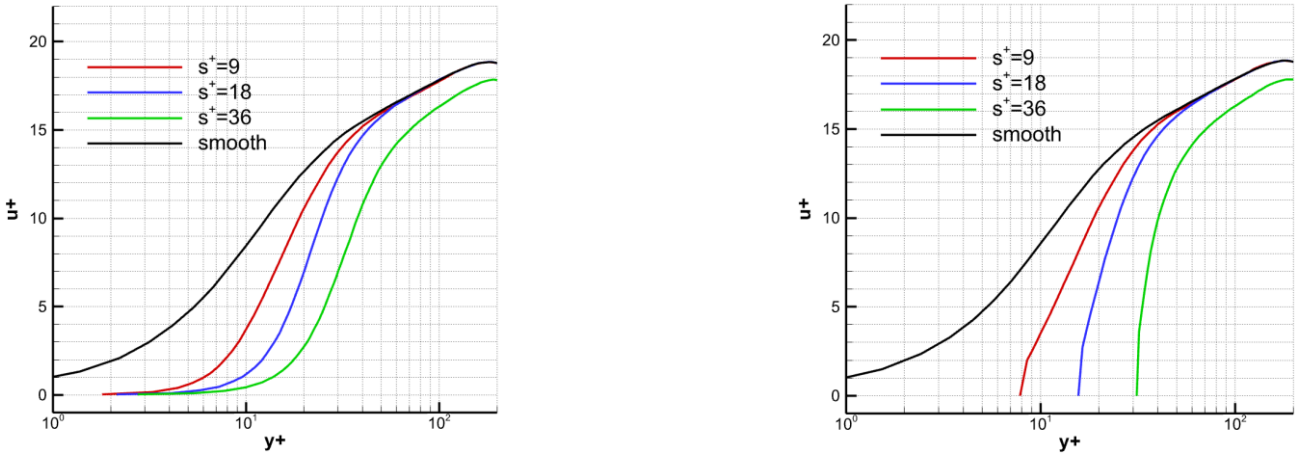

(a)valley (b)tip

Figure 7 – Time-averaged velocity profile at different positions of triangular riblets.

Figure 8 shows time-averaged velocity contours on cross-sections of three types of riblets. There are low-speed fluids in riblets, and these low-speed fluids avoid direct contact between the wall and high-speed fluids in the outer layer. However, low-speed fluid has an obvious effect on the valley of riblets. The wall near the riblets tip is directly exposed to high-speed fluid, which significantly increases shear stress. At the valley, the friction between low-speed fluid and wall produces low shear stress, thereby achieving a drag reduction effect.

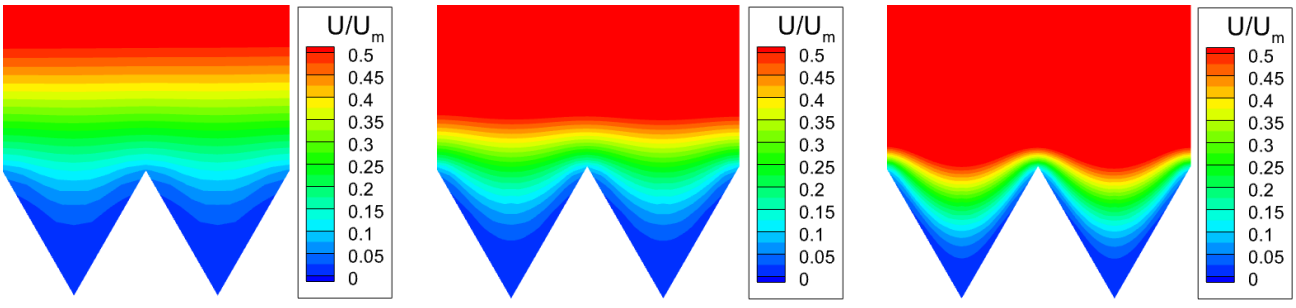

(a) $s^+ = 9$ (b) $s^+ = 18$ (c) $s^+ = 36$

Figure 8 – Time-averaged velocity contour of triangular riblets.

3.3 Second-order statistics

Figures 9 to 11 show the root-mean-square of velocity fluctuation in X, Y and Z direction at valley and tip of triangular riblets. The drag-increasing riblet reduces the velocity fluctuation in the X direction

but enhances the velocity fluctuation in the Y and Z direction. The drag-decreasing riblets are significantly different. The drag-decreasing riblets reduce the root-mean-square velocity fluctuation in the X, Y, and Z direction.

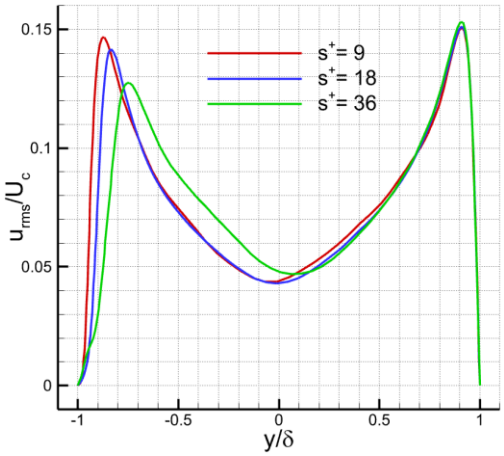

(a) valley

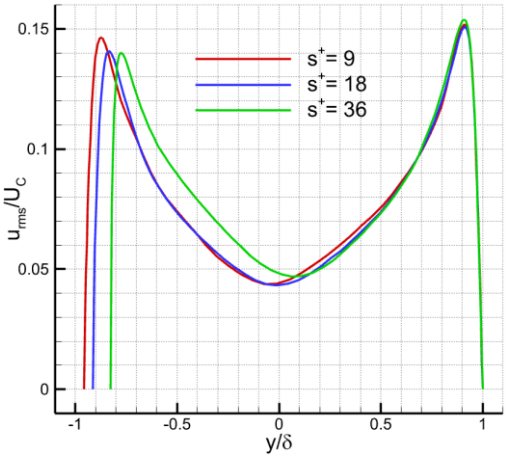

(b) tip

Figure 9 – Root mean square velocity fluctuation in the X direction of triangular riblets.

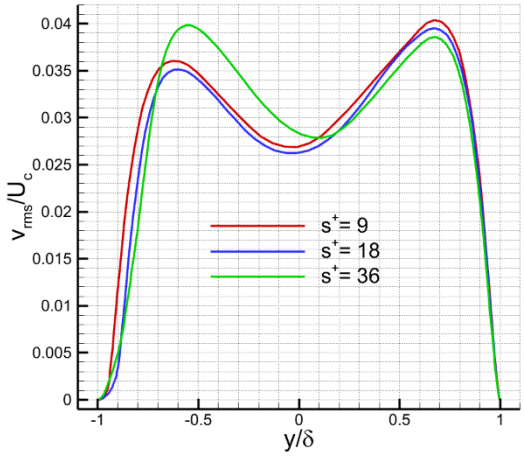

(a) valley

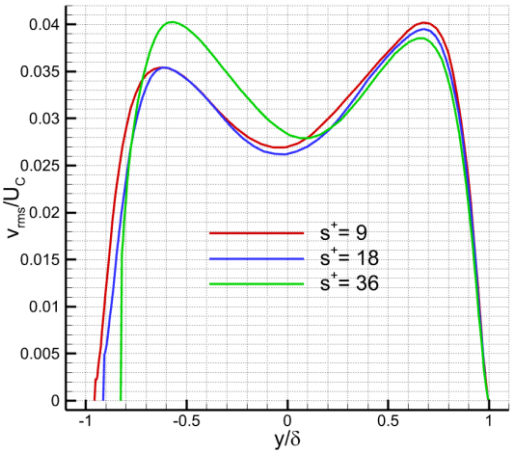

(b) tip

Figure 10 – Root mean square velocity fluctuation in the Y direction of triangular riblets.

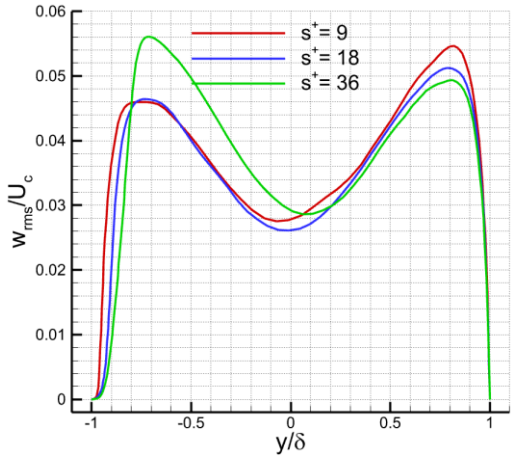

(a) valley

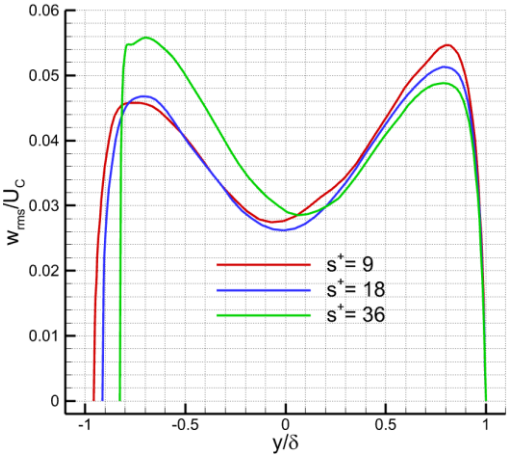

(b) tip

Figure 11 – Root mean square velocity fluctuation in the Z direction of triangular riblets.

Figures 12, 13 and 14 show the distribution of Reynolds shear stress τ_R, viscous shear stress τ_μ

and total shear stress τ_{total} at the valley and tip of triangular riblets. With the increase of riblet size, the peak value of Reynolds shear stress first decreases and then increases. The $s^+ = 18$ riblet reduces the peak value of Reynolds shear stress effectively. For the smooth surface, the viscous shear stress at the wall is the largest and as the observation point moves away from the wall, the viscous shear stress decreases monotonously. For the riblet surface, as the observation point moves away from the wall, the viscous shear stress first increases and then decreases, and a local peak appears near the wall. The peak value of viscous shear stress at the valley of riblets is relatively small, while the peak value near the tip is larger. As the riblet size increases, the peak value of the viscous shear stress at the valley decreases monotonously, while the peak value at the tip increases monotonously.

At the valley of $s^+ = 18$ riblets, the total shear stress peak value is the smallest, so the drag reduction effect is the best. Although $s^+ = 36$ riblets have smaller total shear stress near the wall, the total shear stress is significantly larger than that of drag-reducing riblets far away from the wall, so the drag-increasing effect is achieved. The total shear stress of $s^+ = 9$ riblets is the same as that of $s^+ = 18$ riblets far away from the wall, but the total shear stress near the wall is slightly larger, so the drag reduction effect is reduced. At the tip of riblets, the total shear stress of $s^+ = 36$ riblets is significantly larger than that of drag-reducing riblets.

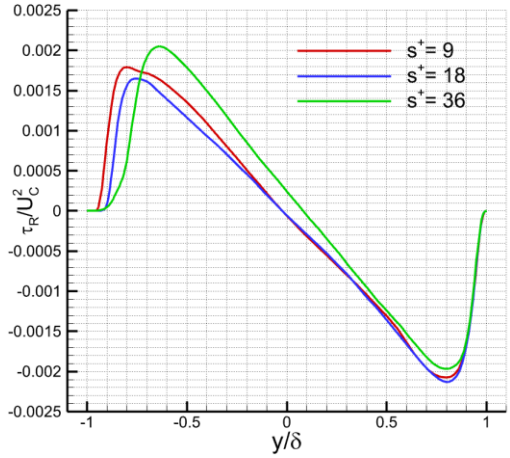

(a) valley

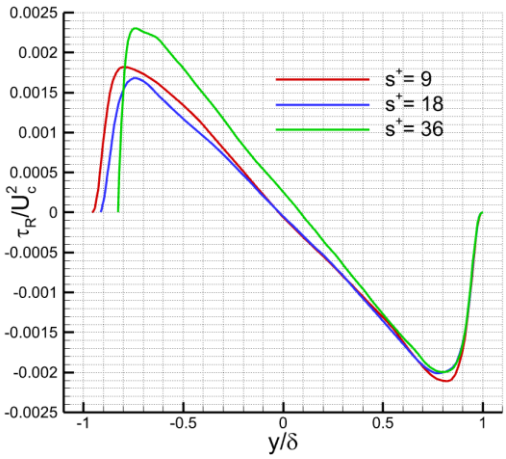

(b) tip

Figure 12 – Reynolds shear stress distribution of triangular riblets.

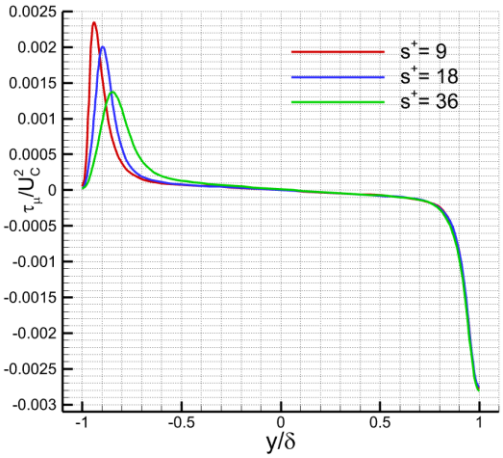

(a) valley

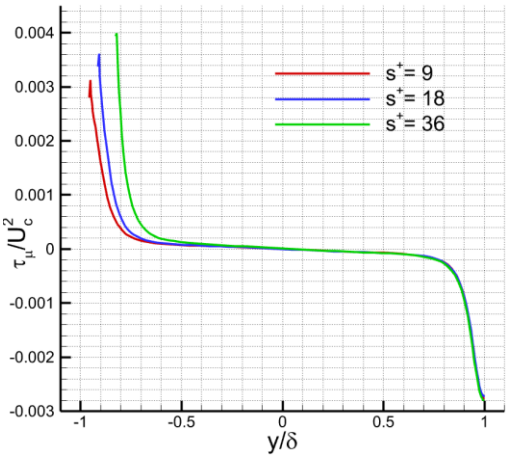

(b) tip

Figure 13 – Viscous shear stress distribution of triangular riblets.

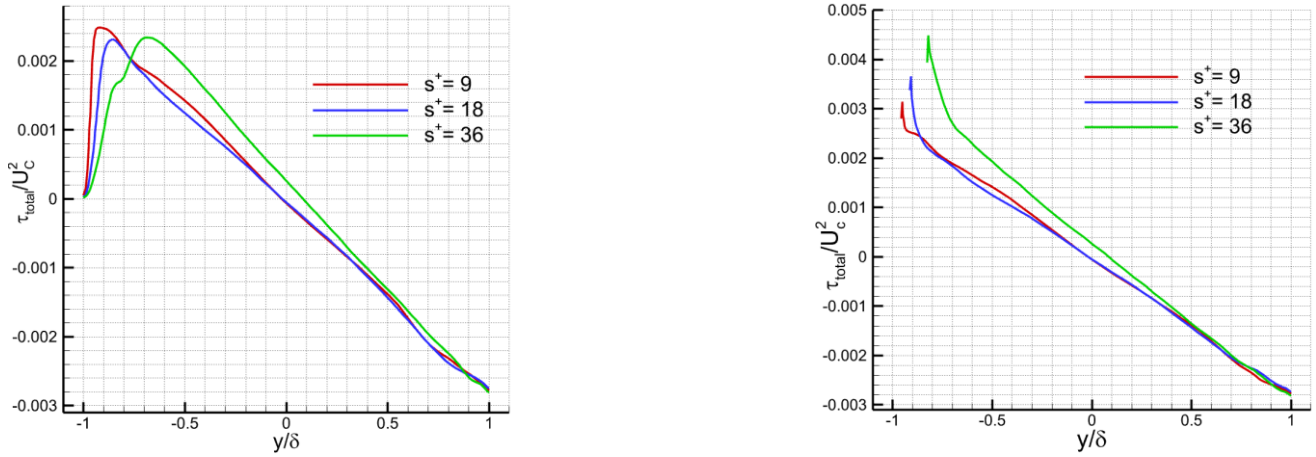

(a) valley (b) tip

Figure 14 – Total shear stress distribution of triangular riblets.

Figure 15 shows the contour of turbulent kinetic energy generation of triangular riblets. Whether it is drag-increasing or drag-reducing riblets, the generation of turbulent kinetic energy inside riblets is effectively suppressed. There are obvious differences in the generation of turbulent kinetic energy at different positions of drag-increasing riblets. The riblet tip is the main generating area of turbulent kinetic energy, and the peak value exceeds the smooth surface. For drag-reducing riblets, the turbulent kinetic energy generation term near the wall is smaller than that of a smooth surface, and the distribution of generic terms is quite uniform. The $s^+ = 18$ riblet has the smallest turbulent kinetic energy generation, while $s^+ = 36$ riblets have the largest. As the riblet size increases, the generation of turbulent kinetic energy gradually approaches the wall, and finally moves inside riblets. In general, compared with the smooth surface, drag-decreasing riblets reduce the generation of turbulent kinetic energy, while the drag-increasing riblets significantly increase the generation terms.

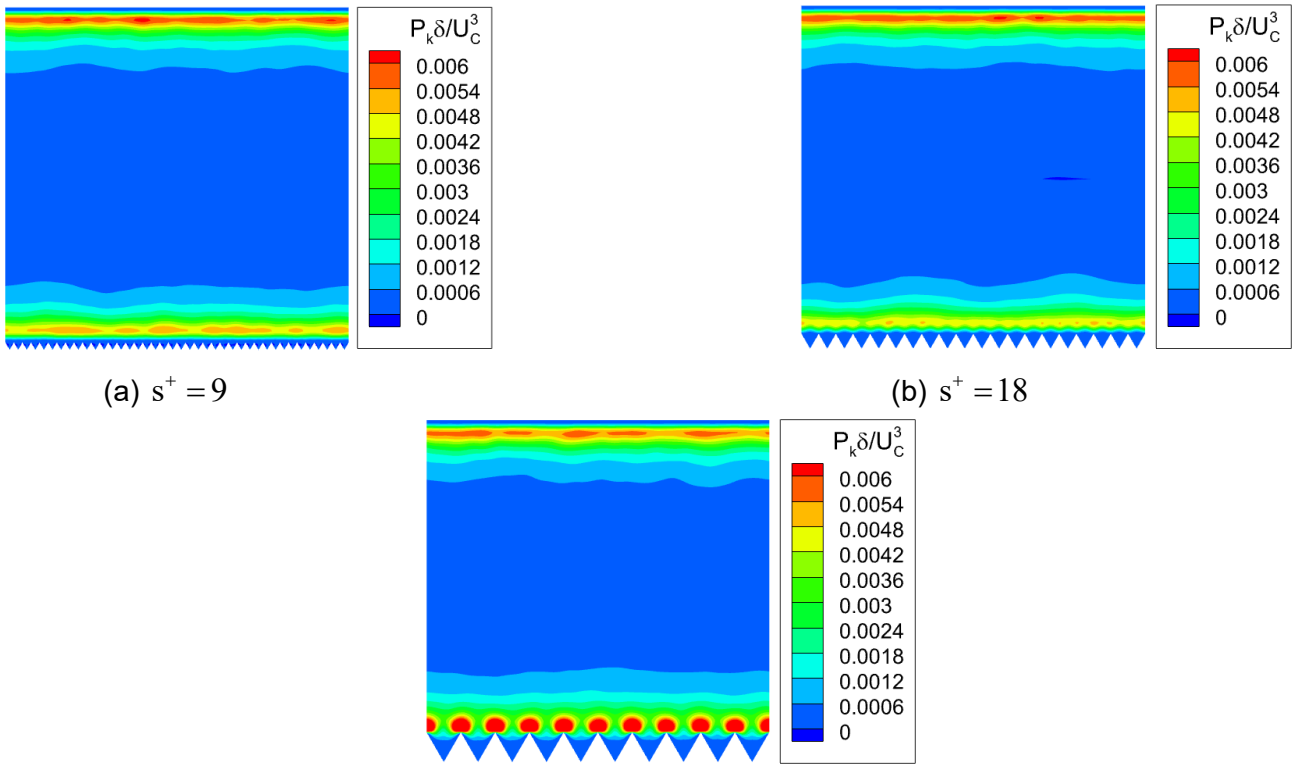

(a) $s^+ = 9$ (b) $s^+ = 18$

(c) $s^+ = 36$

Figure 15 –Turbulent kinetic energy generation of triangular riblets.

3.4 Instantaneous flow field

Figure 16 and Figure 17 show the normal and spanwise velocity fluctuation contours in the XZ plane. For normal and spanwise velocity fluctuation, drag-reducing riblets are significantly lower than drag-increasing riblets. This result is consistent with DNS results of Ng[24] et al. Compared with drag-increasing riblet, drag-reducing riblets could reduce the momentum exchange of fluid in the boundary layer caused by the velocity fluctuation, to achieve a better drag reduction effect.

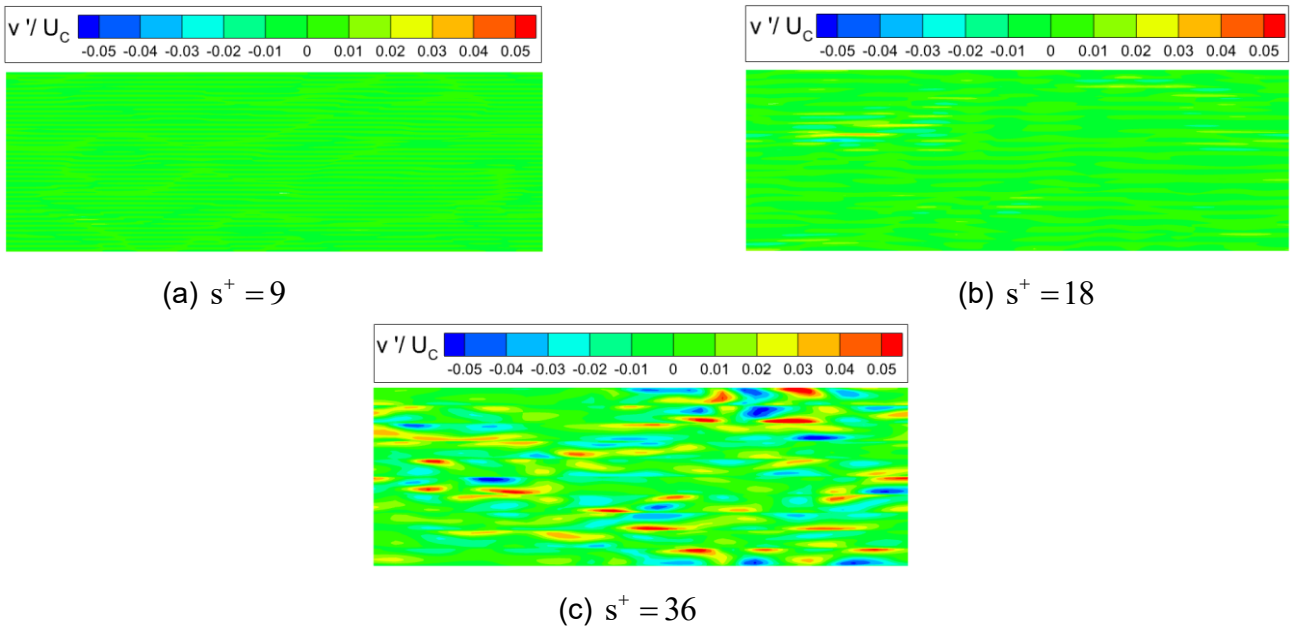

(a) $s^+ = 9$ (b) $s^+ = 18$

(c) $s^+ = 36$

Figure 16 – Contour of normal velocity fluctuation.

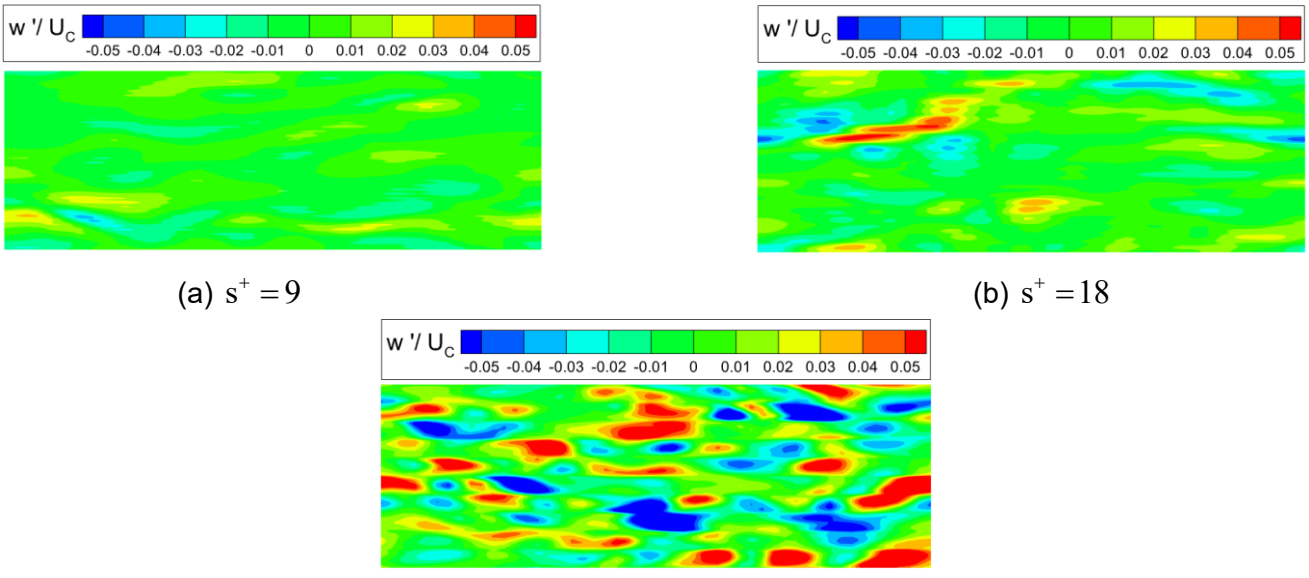

(a) $s^+ = 9$ (b) $s^+ = 18$

(c) $s^+ = 36$

Figure 17 – Contour of spanwise velocity fluctuation.

Figures 18 to 20 show the vortex structure distribution of triangular riblets on the XZ plane. The drag-increasing riblets increase the vortex structure near the wall. The vortex structures near the riblet surface and smooth surface exhibit very different characteristics. With the increase of y+ from 10 to 20, the vortex structure near smooth surface gradually increases and its' amplitude increases, while the vortex structure near the riblet surface decreases and its' amplitude decrease. This indicates that drag-increasing riblet induces complex vortex structure near the wall, and as the observation point

moves away from the wall, the induced vortex structure gradually decreases. Drag-reducing riblets have a smaller effect on the vortex structure near the wall. The distribution of vortex structure near drag-reducing riblets is the same as the smooth surface. The $s^+ = 18$ riblet suppresses the formation of the vortex structure near the wall. By suppressing the generation of vortex structure, the flow stability near the wall is enhanced, to achieve a better drag reduction effect.

(a) $y^+ = 10$ (b) $y^+ = 20$

Figure 18 – Vortex structure distribution near triangular riblets with $s^+ = 9$.

(a) $y^+ = 10$ (b) $y^+ = 20$

Figure 19 – Vortex structure distribution near triangular riblets with $s^+ = 18$.

(a) $y^+ = 10$ (b) $y^+ = 20$

Figure 20 – Vortex structure distribution near triangular riblets with $s^+ = 36$.

4. Conclusion

In this paper, turbulent boundary layer flow field over riblets is numerically simulated based on large eddy simulation method. First, the turbulent channel flow is simulated to verify the accuracy of the numerical method. After that, the turbulent boundary layer flow field over triangular riblets is simulated, and the drag reduction law is summarized. The following conclusions are drawn:

(1) Compared with smooth surface, the velocity profile of drag-increasing riblet has a significant downward shift in the logarithmic region. The velocity profile of drag-reducing riblets is significantly higher than that of drag-increasing riblets and coincides with the velocity profile of

the smooth surface in the logarithmic region. There are low-speed fluids inside triangular riblets, and these low-speed fluids act as a buffer to avoid direct contact between riblets and high-speed fluids in the outer layer. Low-speed fluid has an obvious effect on riblet valley. At the tip of riblets, the fluid velocity is relatively high, which causes a sharp rise in shear stress.

(2) Drag-reducing riblets decrease the velocity fluctuation in streamwise, normal and spanwise directions and Reynolds shear stress. In addition, the drag-reducing riblets suppress the formation of near-wall vortex structure and enhance the flow stability, thus achieving a better drag reduction effect. While drag-increasing riblets decrease velocity fluctuation in the streamwise direction but amplify velocity fluctuation in normal and spanwise directions and Reynolds shear stress. Moreover, the drag-increasing riblets increase the number of vortex structures near the wall, which indicates that drag-increasing riblet induces complex vortex structures.

(3) Whether it is drag-increasing or drag-reducing riblet, the generation of turbulent kinetic energy inside riblets is effectively suppressed. The generation of turbulent kinetic energy at different positions of drag-increasing riblet is quite different. The tip of riblets is the main area of turbulent kinetic energy generation, and the peak value of the generation term exceeds that of the smooth surface. The amplitude of turbulent kinetic energy generation term near drag-reducing riblets is smaller than that of smooth surface, and the distribution of generic term is relatively uniform.

5. Acknowledgment

This work has benefited greatly from the support of the Aeronautic Science Foundation of China under grant 2018ZA53014 and the Open Fund of Key Laboratory of Icing and Anti/De-icing of China under grant IADL20200101.

6. Contact Author Email Address

Mail to: dushuya@mail.nwpu.edu.cn

7. Copyright Statement

References

[1] Ma H D, Cui E J. Drag prediction and reduction for civil transportation aircraft (in Chinese) [J]. *Mechanics in Engineering*, Vol. 29, No.2, pp 1-8,2007.

[2] Zhou LY. Preparation and antifriction properties of shark skin texture (in Chinese)[D].Jiangxi: *Jiangxi University of Science and Technology*, 2018.

[3] Chen H W, Rao F G, and Shang X P. Biomimetic drag reduction study on herringbone riblets of bird feather[J]. *Journal of Bionic Engineering*, Vol. 10, No.3, pp 341-349, 2013.

[4] Walsh M J, Weinstein L M. Drag and heat transfer on surfaces with small longitudinal fins[J]. *11th Fluid and Plasma Dynamics Conference*(AIAA), 1161,1978.

[5] Walsh M J, Lindemann A M. Optimization and application of riblets for turbulent drag reduction [J]. *22nd Aerospace Sciences Meeting* (AIAA), 347, 1984.

[6] Walsh M J. Turbulent boundary layer drag reduction using riblets [J]. *20th Aerospace Sciences Meeting* (AIAA), 169, 1982.

[7] Walsh M J. Viscous drag reduction in boundary layers[J]. *Progress in Astronautics and Aeronautics*, pp 203-261, 1990.

[8] Bechert D W, Bruse M and Hage W. Experiments on drag-reducing surfaces and their optimization with an adjustable geometry[J]. *Journal of Fluid Mechanics*, Vol. 338, pp 59-87, 1997.

[9] Bacher E V, Smith C R. Turbulent boundary-layer modification by surface riblets [J]. *AIAA Journal*, Vol. 24, No.8, pp 1382-1385, 1986.

[10]Choi K S. Near-wall structure of a turbulent boundary layer with riblets [J]. *Journal of Fluid Mechanics*, Vol. 208, pp 417-458, 1989.

[11]Chu D C, Karniadakis G E. A direct numerical simulation of laminar and turbulent flow over riblet-mounted surfaces[J]. *Journal of Fluid Mechanics*, Vol. 250, pp 1-42, 1993.

[12]Choi H, Moin P and Kim J. Direct numerical simulation of turbulent flow over riblets[J]. *Journal of Fluid Mechanics*, Vol. 255, pp 503-539, 1993.

[13]Martin S, Bhushan B. Fluid flow analysis of a shark-inspired microstructure [J]. *Journal of Fluid Mechanics*, Vol. 756, pp 5-29, 2014.

[14]Ng J H, Jaiman R K and Lim T T. Direct numerical simulation of geometric effects on turbulent flows over riblets[J]. *AIAA Flow Control Conference*, 2649, 2014.

[15]Mele B, Tognaccini R, Catalano P. Performance assessment of a transonic wing-body configuration with riblets installed[J]. *Journal of Aircraft*, Vol. 53, No. 1, pp 129-140, 2016.

[16]Choi K S. Smart flow control with riblets[J]. *Advanced Materials Research*, Vol. 745, pp 27-40, 2013.

[17]Abdulbari H A, Mahammed H D and Hassan Z B Y. Bio-inspired passive drag reduction techniques: A review[J]. *ChemBioEng Rev*, Vol. 2, No. 3, pp 185-203, 2015.

[18]Kim J, Moin P and Moser R. Turbulence statistics in fully developed channel flow at low Reynolds number[J]. *Journal of Fluid Mechanics*, Vol. 177, pp 133-166, 1987.

[19]Zhang Z L. Drag reduction mechanism and modeling strategy of two-dimensional shark-skin-inspired riblets in turbulent flows (in Chinese)[D]. Beijing: *University of Chinese Academy of Sciences*, 2020.